https://doi.org/10.1016/j.cej.2020.127900

TiO_2 Film Supported by Vertically Aligned Gold Nanorod Superlattice Array for Enhanced Photocatalytic Hydrogen Evolution

Liangsheng Hu,[a,†] Yong Li,[a,†] Xiang Peng,[b] Weiran Zheng,[a] Wen Xu,[c] Jinyang Zhu,[d] Lawrence Yoon Suk Lee,[a,] Paul K. Chu,[b] and Kwok-Yin Wong[a,*]*

[a] Department of Applied Biology and Chemical Technology and State Key Laboratory of Chemical Biology and Drug Discovery, The Hong Kong Polytechnic University, Hung Hom, Kowloon, Hong Kong SAR, China

[b] Department of Physics and Department of Materials Science and Engineering, City University of Hong Kong, Tat Chee Avenue, Kowloon, Hong Kong SAR, China

[c] State Key Laboratory of Integrated Optoelectronics, College of Electronic Science and Engineering, Jilin University, Changchun, China

[d] State Centre for International Cooperation on Designer Low-Carbon & Environmental Materials, School of Materials Science and Engineering, Zhengzhou University, Zhengzhou, China

[†] L. Hu and Y. Li contributed equally to this work.

ORCID

L. Hu: 0000-0002-4133-2090

L.Y.S. Lee: 0000-0002-6119-4780

K.-Y. Wong: 0000-0003-4984-7109

***Corresponding Authors:**

E-mails: lawrence.ys.lee@polyu.edu.hk (L. Y. S. Lee); kwok-yin.wong@polyu.edu.hk (K.-Y. Wong)

Graphical Abstract

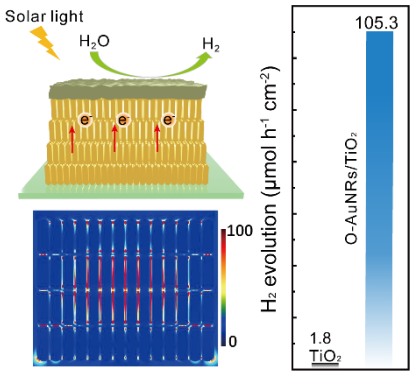

A large area TiO_2 film supported by vertically ordered Au nanorod superlattice array (O-AuNRs/TiO_2) is fabricated on a glass substrate. Compared to both pristine TiO_2 film and the TiO_2 film supported by randomly-oriented AuNRs (R-AuNRs/TiO_2), the O-AuNRs/TiO_2 delivers highly enhanced photocatalytic hydrogen evolution rate, benefiting from the significant localized surface plasmon resonance (LSPR) enhancement by O-AuNRs.

Highlights

- A centimeter-scale TiO_2 film supported by Au nanorod superlattice/ordered array (O-AuNRs/TiO_2) was fabricated on a glass substrate;
- Well-ordered and closely-packed AuNR superlattice dramatically boosts the local electromagnetic field;
- O-AuNRs architecture plays a key role in enhancing the photocatalytic activity of TiO_2 film;
- O-AuNRs/TiO_2 exhibits a highly enhanced photocatalytic hydrogen evolution rate, 58 times of unsupported TiO_2 film.

Abstract

Photocatalytic hydrogen generation from water as a renewable non-polluting technique for converting solar energy to chemical energy has recently attracted worldwide attention. However, low hydrogen production efficiency of traditional photocatalysis still remains as a challenge. Here, we report a large area TiO_2 film supported by vertically ordered Au nanorods superlattice array (O-AuNRs/TiO_2), which demonstrates excellent photocatalytic performances of hydrogen evolution from water under solar and visible light irradiation. The O-AuNRs/TiO_2 architecture enables the significant localized surface plasmon resonance (LSPR) enhancement, including both local electromagnetic field effect and hot electron transfer effect, which promotes the photocatalytic hydrogen evolution rate of the TiO_2 film by 58 times. The photocatalytic efficiency of O-AuNRs/TiO_2 exceeds that of the TiO_2 film supported by randomly oriented AuNRs by over five times. Finite difference time domain (FDTD) modeling results support that the strong coupling of O-AuNRs enhances the electromagnetic field intensity along the longitudinal axis in the gaps between adjacent AuNRs and the average electric field enhancement factors at the interface between the AuNRs and TiO_2 of O-AuNRs/TiO_2. This work demonstrates the substantial performance boost of conventional photocatalyst by LSPR enhancement, thus provides a promising tactic to devise highly efficient photocatalytic system for solar energy conversion.

Keywords: photocatalytic hydrogen evolution; Au nanorod superlattice; surface plasmon resonance; hot electron; near field enhancement

1. Introduction

Photocatalytic hydrogen generation from water has long been considered as one of the most promising future strategies for solar energy-to-chemical fuels conversion. Among various materials developed so far, nanoscale titanium dioxide (TiO_2) is usually regarded as a benchmarking photocatalyst for metal-oxide-based semiconductors and has been substantially investigated for decades.[1, 2] Nevertheless, the relatively large bandgap energy of TiO_2 (3.20 eV for anatase and 3.03 eV for rutile TiO_2) makes its light absorption limited to the ultraviolet (UV) region of electromagnetic spectrum, which accounts for less than 5% of the whole solar spectrum and thus hampers the utilization of solar energy. Over the past years, substantial efforts have been devoted to boost visible light-absorption of TiO_2.[3-7] Recently, plasmon-mediated tactic has been demonstrated to augment the visible light utilization efficiency by means of achieving hot electron injection, improved photoexcitation, and the propelled charge separation in the coupled photocatalyst.

To accomplish efficient utilization of visible light, the nanostructured plasmonic metals (Au, Ag, Cu, and Al) have been widely implemented into various photocatalysts.[8-14] The light response of such composite photocatalysts can be enhanced and tailored by choosing the suitable components or adjusting the size and shape of the metallic nanostructures. This strategy has been also extensively employed to promote the photocatalytic capability of nanostructured TiO_2 by engaging the plasmonic metal nanoparticles (NPs) as light-harvesting antennas, which exhibit unique localized surface plasmon resonance (LSPR) characteristics at visible or even infrared wavelengths.[15-17] The main LSPR enhancement of photocatalytic performance acts through:[18-21] 1) scattering light to increase the average photon path length between the metal NPs and semiconductors thus boosting light trapping by a photocatalyst;[22, 23] 2) direct hot

electron transfer (DHET),[24-28] in which the plasmon-excited electrons on metal (hot electrons) are injected into the conduction band (CB) of neighboring semiconductor over the Schottky barrier; 3) plasmon-induced resonant energy transfer (PRET), which is regarded as a process of transferring the plasmonic oscillation energy from the plasmonic metal nanocrystals to the nearby semiconductor based on local electromagnetic field (LEMF) effect. The PRET accelerates the generation of additional electron-hole pairs and suppresses the recombination of generated charge carriers in the nearby semiconductor,[29-32] thus boosting the photocatalytic performance.[33]

In addition to the nature, shape, and size of the plasmonic metal,[33-35] the intensity of the LEMF is also largely dependent on the local density, the alignment/orientation, and the interparticle gap of metal crystals.[36-40] Benefiting from the collective plasmonic intensity of the LSPR-excited LEMF, 3-dimensional (3D) superlattice array, an ordered assembly of colloidal nanostructures, especially the anisotropic Au nanorods (AuNRs), has shown the extraordinarily enhanced performances in spectroscopies,[41-44] solar cells,[19] and nanoscale light polarizers.[45, 46] Nevertheless, the size of reported 3D superlattices is usually just a few square micrometers, which hinders their application in the fields where a large area is required. In our previous study, we developed a simple and efficient evaporative self-assembly strategy to build millimeter-scale 3D superlattice arrays composed of dense, regular, and vertically aligned AuNRs for surface-enhanced Raman scattering (SERS).[36] Apparently, the millimeter-scale superlattice arrays are too small to be an effective photocatalytic system for hydrogen evolution reaction (HER). Herein, a centimeter-scale AuNR superlattice/ordered array (O-AuNRs) was fabricated on a glass substrate to study how the LEMF and DHET from the underlying O-AuNR array affect the exciton carrier generation in TiO_2. A remarkably enhanced photocatalytic HER rate of the TiO_2 film deposited on top of O-AuNRs by magnetron sputtering (O-AuNRs/TiO_2) was achieved, which exceeds that of bare TiO_2

film by 58 times.

2. Experimental Section

2.1. Chemicals

Chloroauric acid ($HAuCl_4 \cdot 4H_2O$), silver nitrate ($AgNO_3$), sodium chloride (NaCl), hydrochloric acid (HCl), sodium borohydride ($NaBH_4$), sodium hydroxide (NaOH), ascorbic acid (AA), hexadecyltrimethylammonium bromide (CTAB), 11-mercaptoundecylhexaethylene glycol (MUHEG), and triethanolamine (TEOA) were purchased from Sigma-Aldrich. All the chemicals were used as received without further purification.

2.2. Synthesis of AuNRs

Au nanorods (AuNRs) were prepared in an aqueous solution using a seed-mediated growth method as described previously.[36] Briefly, Au seed particles of 3-4 nm diameter were synthesized first by reducing a mixture of $HAuCl_4$ (0.5 mM, 5 mL) and CTAB (0.2 M, 5 mL) with freshly prepared ice-cold $NaBH_4$ (10 mM, 600 μL) under vigorous stirring. The seed solution was incubated at 37 °C for 2 hours before further use. A growth solution was prepared by adding a mixture of $AgNO_3$ (0.1 M, 150 μL) and $HAuCl_4$ (5 mM, 12 mL) to a CTAB solution (0.2 M, 60 mL), followed by the addition of HCl (1.2 M, 150 μL) and AA (10 mM, 5.55 mL) with gentle swirling until the dark orange color disappears. After that, 100 μL of the Au seed solution was rapidly injected to the growth solution followed by gentle mixing for 10 s and kept undisturbed overnight. Finally, the reaction was stopped by centrifuging the resulting AuNR solution at 9,000 rpm for 20 min. The precipitated product (CTAB-AuNRs) was dispersed in Milli-Q water with a concentration of about

0.8 nM according to the extinction coefficient at the longitudinal LSPR wavelength.

2.3. Synthesis of AuNR array

The fabrication of AuNR array involves two steps. The first step is the modification of AuNRs with MUHEG. The CTAB-AuNR solution (18 mL) was purified by centrifugation (9,000 rpm, 15 min) to remove the excess CTAB. The precipitate was then re-suspended in a 36 mL (0.1 mM) MUHEG aqueous solution and stirred (1,000 rpm) at room temperature overnight to yield the AuNRs capped with the mixture of MUHEG and CTAB (MUHEG-AuNRs). The second stage is the self-assembly of MUHEG-AuNRs on an ITO glass slide (water contact angle is *ca*. 40°) to form the MUHEG-AuNR superlattice array. Specifically, the MUHEG-AuNR suspension was concentrated to various concentrations (20, 50, 100, and 200 nM) by centrifugation. A droplet (200 μL) of the MUHEG-AuNR suspension was drop-cast onto the substrate and kept undisturbed at room temperature under high humidity (around 90 %) to slowly evaporate the water. After 10 hours, four-layer AuNR array (ordered AuNRs, O-AuNRs) were assembled on the substrate. For comparison, CTAB-AuNR solution with the same concentration (200 nM) of AuNR was also assembled on a glass with the same procedure (random AuNRs, R-AuNRs).

2.4. Fabrication of TiO_2 and AuNRs/TiO_2 film

Transparent TiO_2 films were deposited on the substrates (ITO glass slide and AuNRs-coated ITO glass slide) using a commercial pulsed DC reactive magnetron sputtering system (AJA International, ATC Orion). The thickness of TiO_2 film was controlled by deposition time (10, 20, 30, and 45 min). Pure argon (99.999%) and oxygen (99.999%) were used as the sputtering and reactive gas, respectively. Metallic titanium (99.995%) was employed as a sputtering target. The base pressure of the deposition chamber was approximately 1×10^{-4} Pa and the flow rates of Ar

and O_2 were kept constant at 20 and 10 standard cubic centimeters per minute (SCCM), respectively, controlled by mass flow meters. The pulsed DC power was kept constant at 100 W. The AuNRs-on-TiO_2 film was prepared by drop-casting 200 μL of 200 nM CTAB-AuNR solution on the surface of TiO_2 film and keeping undisturbed at room temperature under high humidity (around 90 %) to slowly evaporate the water.

2.5. Characterization of the materials

The morphology of the samples was analyzed by a field emission scanning electron microscopy (FE-SEM, FEI Nova 450 Nano) and a scanning transmission electron microscopy (TEM, JEOL JEM-2100F). Crystallographic phases of samples were identified by a powder Xray diffractometer (XRD, Bruker D2 PHASER) with a diffraction angle 2θ ranging from 20 to 80° and scan rate of 10° min^{-1}. The Raman spectra in this study were collected on a Renishaw 2000 Raman spectrometer. The ultraviolet–visible-near infrared (UV-Vis-NIR) absorption spectra of AuNRs solution, TiO_2, and AuNRs/TiO_2 films were determined by the UV–vis absorption and diffuse reflectance spectra on a Cary 4000 UV-visible spectrophotometer equipped with an integrating sphere for diffuse and total reflection measurements. The photoluminescence (PL) spectra were recorded on a PTI QM-TM (Photon Technology International) fluorescence spectrophotometer with an excitation wavelength of 330 nm.

2.6. Photocatalytic hydrogen evolution reaction (HER)

A piece of the catalyst film (2 cm × 1.5 cm) was immersed in an aqueous solution (20 mL) containing 10 vol.% TEOA as a sacrificial agent in a 50 mL round-bottom quartz flask. The flask was then degassed by bubbling with argon for 30 min and sealed. The sample was irradiated by solar light and visible light using a Newport AM1.5 solar simulator (Xe lamp, 150 W) of the light

intensity of 100 mW cm^{-2} without and with an UV-cutoff filter ($\lambda > 400$ nm), respectively. The generated H_2 was analyzed by an Agilent 7890B GC system using N_2 as carrier gas and a thermal conductivity detector.

2.7. Photoelectrochemical analysis

The photocurrent experiments were conducted on a CHI760E potentiostat (CH Instruments Inc., Shanghai, China) using a standard three electrode system with the fabricated TiO_2 and AuNRs/TiO_2 films as the working electrode. A saturated calomel electrode (SCE) and a Pt foil were used as the reference and counter electrodes, respectively. Photocurrent measurements were performed at a 0.4 V bias potential *vs.* SCE using 1.0 M NaOH as the supporting electrolyte. A 300 W Xe lamp with and without a UV-cutoff filter ($\lambda > 400$ nm) was used as the irradiation source.

2.8. Finite-difference time-domain simulations

The local electromagnetic field intensity distribution of AuNR, TiO_2, and AuNRs/TiO_2 films was performed using commercial software with a frequency domain solver based on the three-dimensional finite-difference-time-domain (3D-FDTD) method. The FDTD method is an explicit time marching algorithm used to solve Maxwell's curl equations on a discretized spatial grid. The absorbing boundary conditions of perfectly matched layer were obtained in different directions. A plane wave at a wavelength of 709 nm was launched into the boundary to simulate the distribution of electromagnetic field. The refractive index of AuNRs was set as $n = 0.18 + 4.96i$ at this frequency, and the refractive index of surrounding medium was equal to 1 as air. The electromagnetic field profiles for the O-AuNRs/TiO_2 and R-AuNRs/TiO_2 hybrid samples were

simulated by putting the vertically aligned AuNRs array and random AuNRs under the TiO_2 film (*ca*. 85 nm). The length and diameter of AuNRs are 65 and 21 nm, respectively. The gaps of the vertically aligned AuNRs array is 1.5 nm in both x and y directions. The averaged electromagnetic field enhancement factors for all samples were obtained by calculating the average value of the electromagnetic field intensity enhancement at the interface between AuNRs and TiO_2 in the mesh range.

3. Results and discussion

Among various Au nanostructures, much attention has been paid to those with rod-like shapes due to their unique optical properties and wide applications in optical devices since their first discovery in 1991.[47] Moreover, the surface plasmon propagation of AuNRs mainly takes place along the longitudinal direction, and the LSPR maxima can be easily tuned between 600 and 1200 nm by adjusting the aspect ratio.[48] To enhance the LSPR effect, the AuNRs were modified with specific capping agents (MUHEG/CTAB) and then assembled on a glass substrate to form a superlattice/ordered array (O-AuNRs). For comparison, the randomly distributed AuNRs (R-AuNRs) were also deposited on a glass substrate using the CTAB-capped AuNRs. On the glass substrate with and without AuNR assemblies, TiO_2 films were deposited by magnetron sputtering to prepare TiO_2, R-AuNRs/TiO_2, and O-AuNRs/TiO_2 photocatalysts as depicted in **Fig. 1**.

Fig. 2 shows the TEM images of CTAB-AuNRs and MUHEG-AuNRs, which reveal the uniform morphology of as-prepared AuNRs. Based on the mean value of Gaussian distributions, the average length and diameter of the AuNRs are estimated to be 65 and 21 nm, respectively. It is evident that the CTAB-AuNRs are randomly oriented (**Fig. 2a**), while the AuNRs are self-

assembled in a side-by-side arrangement after the MUHEG modification (**Fig. 2b**). The UV-Vis-NIR absorption spectra measured from the CTAB-AuNR (wine line) and MUHEG-AuNR (olive line) aqueous solutions are presented in **Fig. 2c**. The CTAB-AuNRs exhibit the longitudinal and transverse LSPR band peaks at 742 and 512 nm, respectively, which arise from the oscillation of free electrons due to the interactions with electromagnetic field. The incubation of CTAB-AuNRs in the MUHEG solution results in a partial displacement of CTAB molecules coated on the side facets of AuNRs by MUHEG molecules because of the stronger binding of S atom to Au than that of N atom. This replacement of capping ligands results in a side-by-side self-assembly due to the increased lateral interactions between the side faces that possess a larger surface area than the end face.[49, 50] After the ligand exchange, a strong blue-shift of the longitudinal LSPR band is observed from 742 to 707 nm with a decrease in its intensity. A slight red-shift of the transverse LSPR band is also observed with a mild increase in the intensity.[51] These changes in the longitudinal and transverse LSPR bands suggest the plasmon coupling between the closely spaced AuNRs as well as the decreased aspect ratio as a result of side-by-side assembly of the MUHEG-AuNRs. This is in good agreement with the numerical simulations of model system,[52] in which a clear blue-shift of the longitudinal plasmon band and a red-shift of the transverse plasmon resonance were observed upon the formation of side-by-side AuNRs assembly due to the coupling of the plasmons of the two interacting nanorods.

To assemble a vertically oriented AuNR array on a glass slide using as less AuNRs as possible, a droplet of MUHEG-AuNR solution of various concentrations was drop-cast onto a glass substrate, followed by slow evaporation under high humidity conditions overnight. **Fig. S1** shows the field emission SEM images of the samples obtained from various MUHEG-AuNR solutions of concentrations from 20 to 200 nM. With the 20 nM solution, the AuNRs are not assembled as a

vertical array but scattered in a horizontal orientation, probably due to insufficient amount of AuNRs (**Fig. S1a**). Upon the increase of AuNR concentration to 50 nM, partially oriented AuNR clusters start to appear (highlighted with red rings in **Fig. S1b**). Further increase of MUHEG-AuNRs concentration to 100 nM yields more than half of AuNRs organized into a closely packed hexagonal structure (**Fig. S1c**), and almost all AuNRs are highly aligned with their long axes perpendicular to the substrate at 200 nM (**Fig. S1d**). This oriented AuNR superlattice array is denoted as ordered AuNRs (O-AuNRs) hereinafter. For comparison, 200 nM CTAB-AuNR solution was drop-cast on a glass substrate following the same procedure. The digital photo of sample prepared from CTAB-AuNRs (**Fig. 3a**) displays an obvious brown ring-shaped mark at the peripheral and lighter color in the central area of the formed film. The corresponding SEM images in **Fig. 3b** and **3c** reveal that the majority of the CTAB-AuNRs are horizontally self-assembled at the rim, while a small amount of aligned CTAB-AuNRs are randomly scattered in the inner area (named as R-AuNRs). In contrast, the photographic image of sample obtained from 200 nM MUHEG-AuNR solution (**Fig. 3d**) shows an even distribution of dark yellow color over the entire film area. The SEM images display that the MUHEG-AuNRs are vertically aligned in the center (**Fig. 3e**) and quasi-aligned at the rim (**Fig. 3f**). The TEM images of the self-assembled MUHEG-AuNR film scraped from glass substrate (**Fig. S2**) further confirm the observations of SEM analyses. Most regions of the film consist of quadruple layers of AuNRs, while the outermost region shows single AuNR array. Such variation in the number of AuNR layer can be correlated to the concentration change of AuNR solution during water evaporation. Initially, the rate of water evaporation is faster than that of AuNR assembly on the substrate due to low concentration of AuNR solution. As water evaporates over time, these two processes reach a balance that the concentration of the AuNRs remains unchanged to assemble into quadruple AuNRs layers for most

area of the film.

On the other hand, the coffee-ring pattern of CTAB-AuNRs is the results of the edgeward flow and pinned contact line, which drive the interior-to-exterior water flow to replenish the evaporated water at the edge. This causes almost all AuNRs to migrate with the edgeward flow and accumulate near the pinned contact line, forming a coffee-ring pattern.[53] The positively charged surface of CTAB-AuNRs repels one another, hindering the self-assembly (**Fig. 1a**). The partial replacement of CTAB with negatively charged MUHEG considerably reduces the electrostatic repulsion and induces the side-by-side self-assembly of AuNRs.[50, 54] The Marangoni effect induces the circulatory flow during the evaporation of the MUHEG-AuNRs droplet,[55] which suppresses the migration of AuNRs to the contact line and redistributes them in the central region. During the slow water evaporation, MUHEG-AuNRs are self-assembled on the glass to form the superlattice arrays, as illuminated in **Fig. 1b**. For the formation of a large scale AuNRs arrays, the following points should be considered: 1) the surface of AuNRs should possess both positively and negatively charged ligands with a suitable surface potential; 2) the substrate should be hydrophilic to allow the droplet containing AuNRs to spread out; 3) high humidity environment is needed to slow down the rate of water evaporation and induce the formation of superlattice array; 4) the concentration of AuNRs solution is important to balance the rate of water evaporation and the fix the AuNRs on the substrate.

On top of these R-AuNRs and O-AuNRs as well as bare glass slide, we sputtered thin layer of TiO_2 controlling its thickness with the deposition time. The thickness of TiO_2 layer influence the photocatalytic HER performance because it would determine the number of active sites as well as the amount of light that reaches AuNRs underneath. The cross-sectional SEM images (**Fig. 4a-d**) show that the thickness of deposited TiO_2 layer increases incrementally from 30 to 123 nm as the

deposition time was increased from 10 to 45 min. The top-view SEM image of the TiO_2 film (**Fig. 4e**) reveals that it consists of numerous nanoparticles of uniform size between 10 to 25 nm, forming a mesoporous structure. **Fig. 4f** compares the photocatalytic HER performance of pristine TiO_2 film (black line) and R-AuNRs/TiO_2 film (wine line) with the variation of TiO_2 thickness. The HER rate of TiO_2 film gradually increases from 1.5 to 2.3 μmol h^{-1} cm^{-2} with the TiO_2 film thickness due to the increased number of catalytic sites. However, in the case of R-AuNRs/TiO_2 heterostructure, the HER rate increases with TiO_2 thickness, reaching the highest rate of 18.2 μmol h^{-1} cm^{-2} at 85 nm, but slightly drops when the thickness of TiO_2 film further increases to 123 nm. Such decline in photocatalytic activity can be correlated with the fact that electromagnetic near field at the plasmon resonance only extends up to 100 nm from the plasmonic metal surface.[30] Although the TiO_2 layer thicker than 100 nm can offer more photocatalytic sites, but it could also cause the shading effect that lowers the LSPR effects from AuNRs. Based on the HER performance results of R-AuNRs/TiO_2, the optimal thickness of TiO_2 layer was determined to be *ca*. 85 nm, and the O-AuNRs/TiO_2 heterostructure was fabricated with this optimum thickness of TiO_2 layer. The low-magnification cross-sectional SEM image of the O-AuNRs/TiO_2 (**Fig. S3a**) displays that the AuNRs layer is slightly thinner near the rim area, while the TiO_2 layer appears to have a uniform thickness over the entire area. The higher magnification SEM images clearly reveals that a monolayer AuNR array is formed at the outermost rim area (**Fig. S3b**) and the quadruple layer of AuNR arrays are formed in the center area (**Fig. 5b** and **S3e**). Double and triple layers of AuNPs are also found in the intermediate areas (**Fig. S3c** and **S3d**). The AuNRs in both monolayer and multilayers are well aligned perpendicularly to the substrate. On the other hand, the typical cross-sectional SEM image taken at the center of the R-AuNRs/TiO_2 film (**Fig. 5a**) shows just a few scattered AuNRs between the uniform TiO_2 layer and the glass substrate, which is consistent with

the result of CTAB-AuNR film on a glass (**Fig. 3b**).

Fig. 6a and **S4** compare the photocatalytic HER performances of TiO_2, R-AuNRs/TiO_2, and O-AuNRs/TiO_2 films. Under the simulated sunlight, the HER rate of O-AuNRs/TiO_2 film is 105.3 μmol h^{-1} cm^{-2} (equivalent to 3,253.8 μmol h^{-1} $g_{(TiO2)}^{-1}$ based on the weight of TiO_2), which is 58 and 5.8 times higher than those obtained from TiO_2 film (1.8 μmol h^{-1} cm^{-2}) and R-AuNRs/TiO_2 film (18.2 μmol h^{-1} cm^{-2}), respectively. Under the visible-light irradiation, the pure TiO_2 film produces negligible amount of H_2, while both R- and O-AuNRs/TiO_2 films exhibit the HER photoactivity with the rates of 3.7 and 30.8 μmol h^{-1} cm^{-2}, respectively. These HER rates of O-AuNRs/TiO_2 film outperforms most recent photocatalysts based on Au and TiO_2 (**Table S1** and **S2**). The durability of the O-AuNRs/TiO_2 was evaluated by a long-term photocatalytic HER where the 90 min-cycle was repeated for 7 times (**Fig. 6b**). The O-AuNRs/TiO_2 film shows a steady H_2 production rate for entire cycles. During a continuous 8 hour-reaction, the volume of hydrogen generated on the O-AuNRs/TiO_2 film linearly increases with the irradiation time, demonstrating its stability (**Fig. S5**).

Apparently, the insertion of AuNRs underneath TiO_2 film drastically elevates the photocatalytic HER activity of TiO_2 film. Considering that no hydrogen is produced when only R- or O-AuNRs film is used, this enhancement arises from the LSPR effects that include the injection of photo-excited hot electrons from the surface of AuNRs to TiO_2, local electromagnetic field (near field) enhancement, and the charge separation in TiO_2 under the simulated solar light irradiation [15, 31] (**Fig. 7a**). The light scattering may also enhance the average length of photon path between the AuNPs and the TiO_2. Under the visible light irradiation, no electron–hole pair will be generated in TiO_2, and thus only LSPR-induced hot electrons from AuNRs are injected to the CB of TiO_2 for HER activity (**Fig. 7b**).

It is worth noting that O-AuNRs/TiO_2 film demonstrates 5.8 and 8.3 times higher HER rates compared with R-AuNRs/TiO_2 film under solar and visible light irradiation, respectively. **Fig. 8a** compares the UV-vis diffuse reflectance spectra of TiO_2 (black line), R-AuNRs/TiO_2 (wine line), and O-AuNRs/TiO_2 (olive line). As previously reported,[56] anatase TiO_2 absorbs only in the UV-light range ($\lambda \leq 375$ nm).[56] In contrast, both R- and O-AuNRs/TiO_2 show significantly enhanced absorptions in the visible range (400 – 800 nm) with the main absorption peaks located at *ca*. 505 and 710 nm, respectively. Noticeably, the LSPR bands of both R- and O-AuNRs/TiO_2 composites show slight blueshifts from those of CTAB- and MUHEG-AuNRs (**Fig. 2c**), which can be ascribed to the change in the dielectric constant of surroundings of AuNRs (refractive index of water = 1.33; anatase TiO_2 = 2.57).[57] In addition, the O-AuNRs/TiO_2 exhibits the stronger longitudinal absorption at *ca*. 709 nm than the R-AuNRs/TiO_2, which is benefited from the stronger coupling of the adjacent O-AuNRs. Such enhanced light absorption of the O-AuNRs/TiO_2 would contribute to photocatalytic HER performance.[58]

To better understand photo-response process, the photoelectrochemical and optical properties were characterized by photocurrent response test, photoluminescence (PL), and Raman spectroscopy. **Fig. 8b** and **S6** present the photocurrent profiles of anatase TiO_2, R- and O-AuNRs/TiO_2 recorded at a bias potential of 0.4 V *vs.* SCE under solar and visible light irradiation, respectively. The O-AuNRs/TiO_2 exhibits much higher photocurrent intensities under both solar and visible light irradiations compared with pristine TiO_2 and R-AuNRs/TiO_2, which clearly illustrates highly boosted interfacial charge transfer and photoelectric conversion rates under solar light irradiation as well as the enhanced LSPR hot electrons generation under visible light irradiation. This is confirmed by steady-state PL spectroscopies shown in **Fig. 8c**. The emission intensity increases in the order of TiO_2, R-AuNRs/TiO_2, and the O-AuNRs/TiO_2, indicating that

more LSPR-induced electron–hole pairs are created and the non-radiative transition channel is suppressed in the O-AuNRs/TiO_2.[37]

The higher enhancement effect of O-AuNRs/TiO_2 is closely related with the orientation of AuNRs. Firstly, the O-AuNR array allows more AuNRs to directly contact the TiO_2 for efficient injection of hot electrons, especially the tips of AuNRs that induce the longitudinal mode LSPR effect (**Fig. 5**).[24-28, 59] It is believed that the longitudinal mode can generate more LSPR hot electrons from the tips than transverse mode from the sides of AuNRs.[17, 60] More importantly, the well-ordered and closely-packed O-AuNR array can narrow the inter-particle gap (*ca*. 1.5 nm, **Fig. S2**), thus forming a chain-like end-to-end AuNR configuration that dramatically boosts hot electron generation at plasmonic hot spots between AuNRs.[61, 61] This can be confirmed by the much enhanced HER performance and photocurrent of O-AuNRs/TiO_2 under visible light irradiation (**Fig. S6**), in which only the direct hot electron transfer effect is working because TiO_2 cannot be activated. Compared with R-AuNRs, such well-organized O-AuNR superlattice of narrow inter-particle gap can induce much stronger local electromagnetic field along the longitudinal direction of adjacent AuNRs.[10, 62-64] The LSPR-induced local electromagnetic field of plasmonic metals increases the amount of photo-generated electron−hole pairs because the photon absorption is proportional to the electric field squared ($|E|^2$),[35] and also facilitates the separation of photo-generated charge carriers in semiconductors, thus enhancing the photocatalytic performance.[29-32, 58, 65] This can explain the dramatic HER enhancement of O-AuNRs/TiO_2 under solar light illumination.

The Raman spectra collected from the bare TiO_2 film and the center and rim of R- and O-AuNRs/TiO_2 films (**Fig. 8d**) further support the proposed enhancement mechanism of H_2 evolution. The Raman signal from the O-AuNRs/TiO_2 matches well with the characteristic Raman bands of

the anatase TiO_2 (A-TiO_2) phase, which feature three E_g peaks at 144, 196, and 638 cm^{-1}, B_{1g} peak at 399 cm^{-1}, and A_{1g} peak at 520 cm^{-1}.[66] Such Raman signals are absent in the spectrum of bare TiO_2 film of the same thickness, which could be due to the low crystallinity of sputtered TiO_2 film as indicated by its amorphous XRD patterns (**Fig. S7**). In the case of R-AuNRs/TiO_2, a weak peak corresponding to E_g band of A-TiO_2 phase is identified at 144 cm^{-1} from the center area, of which the intensity is *ca*. 5.3 times higher than that observed from the rim of R-AuNRs/TiO_2. It is well known that the Raman signal shows highly nonlinear correlation with the intensity of electromagnetic field, and thus the enhanced Raman signals indicate the elevated local electromagnetic field of O-AuNRs/TiO_2.[40, 61, 67, 68] To elucidate the exact extent of electromagnetic field amplification, we engaged FDTD modeling to simulate the electromagnetic field enhancement at the interface between AuNRs and TiO_2 under an incident plane wave along the z direction at the wavelength of LSPR peak (709 nm). As presented in **Fig. 9**, the electromagnetic field intensity along the longitudinal axis in the gaps between adjacent AuNRs is significantly boosted, and the averaged electric field enhancement factors ($\overline{|E|^2 \,/\, |E_0|^2}$) at the interface between the AuNRs and TiO_2 of O-AuNRs/TiO_2 (**Fig. 9a** and **9b**) are much stronger than those of R-AuNRs/TiO_2 (**Fig. 9c** and **9d**). It indicates that the well-ordered and closely-packed O-AuNR array possessing a strong nano-antenna effect shows much stronger local electromagnetic field intensity than R-AuNRs, owing to the coupling effect among the vertically aligned AuNRs.

Another control experiment was conducted by depositing the same amount of CTAB-AuNRs (200 μL of 200 nM CTAB-AuNR solution) on the top surface of TiO_2 film forming a AuNRs-on-TiO_2 configuration and evaluating its photocatalytic properties. Similar to R-AuNRs on the glass, the AuNRs-on-TiO_2 forms a coffer-ring pattern (**Fig. S8a**). The corresponding SEM images reveal that the majority of the AuNRs are horizontally self-assembled at the peripheral region (**Fig. S8b**)

and few AuNRs lie at the inner area (**Fig. S8c**), which is similar to the R-AuNRs on the glass. The HER rates of AuNRs-on-TiO_2 film are 31.3 and 8.2 μmol h^{-1} cm^{-2} under solar and visible light irradiation, respectively (**Fig. S9**), which are higher than those obtained from R-AuNRs/TiO_2 but much lower than those from O-AuNRs/TiO_2. The AuNRs on top of TiO_2 can absorb incident light more than those in R-AuNRs/TiO_2, thus generating more hot electrons in AuNRs. However, the LSPR enhancement of AuNRs-on-TiO_2 is still much weaker than that of O-AuNRs/TiO_2. This is further confirmed by the PL spectra (**Fig. S10**) and FDTD modeling (**Fig. S11**) where the AuNRs-on-TiO_2 shows intermediate PL intensity and local electromagnetic field intensity between the R-AuNRs/TiO_2 and O-AuNRs/TiO_2.

4. Conclusions

In summary, a large area of vertically ordered AuNRs (O-AuNRs) superlattice array was prepared on a glass substrate by a simple evaporative self-assembly method. A layer of anatase TiO_2 film was then deposited on the AuNR superlattice array by magnetron sputtering to form an O-AuNRs/TiO_2 heterogeneous nanostructure. The O-AuNRs/TiO_2 architecture significantly enhances the photocatalytic H_2 evolution rate of the TiO_2 film by 58 times, benefiting from the localized surface plasmon resonance (LSPR) enhancement by the O-AuNRs, including both local electromagnetic field effect and hot electron transfer effect. The dramatically enhanced photoactivity of TiO_2 film supported by O-AuNRs presents a possible pathway to more efficient utilization of the solar energy.

Acknowledgements

This work is financially supported by the Innovation and Technology Commission of Hong Kong to the State Key Laboratory of Chemical Biology and Drug Discovery, The Hong Kong Polytechnic University, and National Natural Science Foundation of China (21806099). KYW acknowledges the support from the Patrick S.C. Poon Endowed Professorship.

Appendix A. Supplementary data

Supplementary material related to this article can be found, in the online version, at doi: https:

References

[1] Q. Wang, K. Domen, Particulate photocatalysts for light-driven water splitting: Mechanisms, challenges, and design strategies, Chem. Rev., 120 (2020) 919-985.

[2] S.T. Kochuveedu, Y.H. Jang, D.H. Kim, A study on the mechanism for the interaction of light with noble metal-metal oxide semiconductor nanostructures for various photophysical applications, Chem. Soc. Rev., 42 (2013) 8467-8493.

[3] Y. Ma, X.L. Wang, Y.S. Jia, X.B. Chen, H.X. Han, C. Li, Titanium dioxide-based nanomaterials for photocatalytic fuel generations, Chem. Rev., 114 (2014) 9987-10043.

[4] S.U. Khan, M. Al-Shahry, W.B. Ingler, Jr., Efficient photochemical water splitting by a chemically modified N-TiO_2, Science, 297 (2002) 2243-2245.

[5] L.S. Hu, K.F. Huo, R.S. Chen, B. Gao, J.J. Fu, P.K. Chu, Recyclable and high-sensitivity electrochemical biosensing platform composed of carbon-doped TiO_2 nanotube arrays, Anal. Chem., 83 (2011) 8138-8144.

[6] Y. Li, Y.-K. Peng, L. Hu, J. Zheng, D. Prabhakaran, S. Wu, T.J. Puchtler, M. Li, K.-Y. Wong, R.A. Taylor, S.C.E. Tsang, Photocatalytic water splitting by N-TiO_2 on MgO (111) with exceptional quantum efficiencies at elevated temperatures, Nat. Commun., 10 (2019) 4421.

[7] L. Hu, Y. Li, W. Zheng, Y.-K. Peng, E. Tsang, L.Y.S. Lee, K.-y. Wong, Blue ordered/disordered janus-type TiO_2 nanoparticles for enhanced photocatalytic hydrogen generation, J. Mater. Chem. A, (2020). http://dx.doi.org/10.1039/D0TA06281B.

[8] E. Ha, L.Y.S. Lee, J.C. Wang, F.H. Li, K.Y. Wong, S.C.E. Tsang, Significant enhancement in photocatalytic reduction of water to hydrogen by Au/Cu_2ZnSnS_4 nanostructure, Adv. Mater., 26 (2014) 3496-3500.

[9] E. Ha, L.Y.S. Lee, H.W. Man, S.C.E. Tsang, K.Y. Wong, Morphology-controlled synthesis of Au/Cu_2FeSnS_4 core-shell nanostructures for plasmon-enhanced photocatalytic hydrogen generation, ACS Appl. Mater. Interfaces, 7 (2015) 9072-9077.

[10] S. Linic, P. Christopher, D.B. Ingram, Plasmonic-metal nanostructures for efficient conversion of solar to chemical energy, Nat. Mater., 10 (2011) 911.

[11] C. Wang, D. Astruc, Nanogold plasmonic photocatalysis for organic synthesis and clean energy conversion, Chem. Soc. Rev., 43 (2014) 7188-7216.

[12] Z. Li, L. Shi, D. Franklin, S. Koul, A. Kushima, Y. Yang, Drastic enhancement of photoelectrochemical water splitting performance over plasmonic Al@TiO_2 heterostructured nanocavity arrays, Nano Energy, 51 (2018) 400-407.

[13] L. Guo, C. Zhong, J. Cao, Y. Hao, M. Lei, K. Bi, Q. Sun, Z.L. Wang, Enhanced photocatalytic

H_2 evolution by plasmonic and piezotronic effects based on periodic Al/$BaTiO_3$ heterostructures, Nano Energy, 62 (2019) 513-520.

[14] J. Zhu, M. Zhang, J. Xiong, Y. Yan, W. Li, G. Cheng, Electrostatically assembled construction of ternary TiO_2-Cu@C hybrid with enhanced solar-to-hydrogen evolution employing amorphous carbon dots as electronic mediator, Chem. Eng. J., 375 (2019) 121902.

[15] H. Li, Z. Bian, J. Zhu, Y. Huo, H. Li, Y. Lu, Mesoporous Au/TiO_2 nanocomposites with enhanced photocatalytic activity, J. Am. Chem. Soc., 129 (2007) 4538-4539.

[16] C.H. Fang, H.L. Jia, S. Chang, Q.F. Ruan, P. Wang, T. Chen, J.F. Wang, (Gold core)/(titania shell) nanostructures for plasmon-enhanced photon harvesting and generation of reactive oxygen species, Energy Environ. Sci., 7 (2014) 3431-3438.

[17] B.H. Wu, D.Y. Liu, S. Mubeen, T.T. Chuong, M. Moskovits, G.D. Stucky, Anisotropic growth of TiO_2 onto gold nanorods for plasmon-enhanced hydrogen production from water reduction, J. Am. Chem. Soc., 138 (2016) 1114-1117.

[18] S.K. Cushing, N. Wu, Progress and perspectives of plasmon-enhanced solar energy conversion, J. Phys. Chem. Lett., 7 (2016) 666-675.

[19] M.J. Rozin, D.A. Rosen, T.J. Dill, A.R. Tao, Colloidal metasurfaces displaying near-ideal and tunable light absorbance in the infrared, Nat. Commun., 6 (2015) 7325.

[20] Y.H. Jang, Y.J. Jang, S. Kim, L.N. Quan, K. Chung, D.H. Kim, Plasmonic solar cells: from rational design to mechanism overview, Chem. Rev., 116 (2016) 14982-15034.

[21] N.N. Jiang, X.L. Zhuo, J.F. Wang, Active plasmonics: Principles, structures, and applications, Chem. Rev., 118 (2018) 3054-3099.

[22] J.A. Schuller, E.S. Barnard, W. Cai, Y.C. Jun, J.S. White, M.L. Brongersma, Plasmonics for extreme light concentration and manipulation, Nat. Mater., 9 (2010) 193.

[23] R.A. Pala, J.S. Liu, E.S. Barnard, D. Askarov, E.C. Garnett, S. Fan, M.L. Brongersma, Optimization of non-periodic plasmonic light-trapping layers for thin-film solar cells, Nat. Commun., 4 (2013) 2095.

[24] A. Furube, L. Du, K. Hara, R. Katoh, M. Tachiya, Ultrafast plasmon-induced electron transfer from gold nanodots into TiO_2 nanoparticles, J. Am. Chem. Soc., 129 (2007) 14852-14853.

[25] C.u. Gomes Silva, R. Juárez, T. Marino, R. Molinari, H. García, Influence of excitation wavelength (UV or visible light) on the photocatalytic activity of titania containing gold nanoparticles for the generation of hydrogen or oxygen from water, J. Am. Chem. Soc., 133 (2010) 595-602.

[26] C. Clavero, Plasmon-induced hot-electron generation at nanoparticle/metal-oxide interfaces for photovoltaic and photocatalytic devices, Nat. Photonics, 8 (2014) 95-103.

[27] K. Aydin, V.E. Ferry, R.M. Briggs, H.A. Atwater, Broadband polarization-independent resonant light absorption using ultrathin plasmonic super absorbers, Nat. Commun., 2 (2011) 517.

[28] Y. Yu, K.D. Wijesekara, X.X. Xi, K.A. Willets, Quantifying wavelength-dependent plasmonic hot carrier energy distributions at metal/semiconductor interfaces, ACS Nano, 13 (2019) 3629-3637.

[29] M.W. Knight, H. Sobhani, P. Nordlander, N.J. Halas, Photodetection with active optical antennas, Science, 332 (2011) 702-704.

[30] D.B. Ingram, S. Linic, Water splitting on composite plasmonic-metal/semiconductor photoelectrodes: evidence for selective plasmon-induced formation of charge carriers near the semiconductor surface, J. Am. Chem. Soc., 133 (2011) 5202-5205.

[31] S.K. Cushing, J. Li, F. Meng, T.R. Senty, S. Suri, M. Zhi, M. Li, A.D. Bristow, N. Wu, Photocatalytic activity enhanced by plasmonic resonant energy transfer from metal to semiconductor, J. Am. Chem. Soc., 134 (2012) 15033-15041.

[32] J. Li, S.K. Cushing, F. Meng, T.R. Senty, A.D. Bristow, N. Wu, Plasmon-induced resonance energy transfer for solar energy conversion, Nat. Photonics, 9 (2015) 601-607.

[33] R. Jiang, B. Li, C. Fang, J. Wang, Metal/semiconductor hybrid nanostructures for plasmon-enhanced applications, Adv. Mater., 26 (2014) 5274-5309.

[34] X. Zhang, Y.L. Chen, R.-S. Liu, D.P. Tsai, Plasmonic photocatalysis, Rep. Prog. Phys., 76 (2013) 046401.

[35] W. Hou, S.B. Cronin, A review of surface plasmon resonance-enhanced photocatalysis, Adv. Funct. Mater., 23 (2013) 1612-1619.

[36] P.H. Li, Y. Li, Z.K. Zhou, S.Y. Tang, X.F. Yu, S. Xiao, Z.Z. Wu, Q.L. Xiao, Y.T. Zhao, H.Y. Wang, P.K. Chu, Evaporative self-assembly of gold nanorods into macroscopic 3D plasmonic superlattice arrays, Adv. Mater., 28 (2016) 2511-2517.

[37] R. Shi, Y.H. Cao, Y.J. Bao, Y.F. Zhao, G.I.N. Waterhouse, Z.Y. Fang, L.Z. Wu, C.H. Tung, Y.D. Yin, T.R. Zhang, Self-assembled Au/CdSe nanocrystal clusters for plasmon-mediated photocatalytic hydrogen evolution, Adv. Mater., 29 (2017) 1700803.

[38] Z. Yin, D.L. Zhou, W. Xu, S.B. Cui, X. Chen, H. Wang, S.H. Xu, H.W. Song, Plasmon-enhanced upconversion luminescence on vertically aligned gold nanorod monolayer supercrystals, ACS Appl. Mater. Interfaces, 8 (2016) 11667-11674.

[39] J. Xu, W.M. Yang, S.J. Huang, H. Yin, H. Zhang, P. Radjenovic, Z.L. Yang, Z.Q. Tian, J.F. Li, CdS core-Au plasmonic satellites nanostructure enhanced photocatalytic hydrogen evolution reaction, Nano Energy, 49 (2018) 363-371.

[40] S.Y. Ding, E.M. You, Z.Q. Tian, M. Moskovits, Electromagnetic theories of surface-enhanced Raman spectroscopy, Chem. Soc. Rev., 46 (2017) 4042-4076.

[41] H.Y. Wang, L. Yao, X. Mao, K. Wang, L.H. Zhu, J.T. Zhu, Gold nanoparticle superlattice monolayer with tunable interparticle gap for surface-enhanced Raman spectroscopy, Nanoscale, 11 (2019) 13917-13923.

[42] Q.Q. Shi, D.E. Gomez, D.S. Dong, D. Sikdar, R.F. Fu, Y.Y. Liu, Y.M. Zhao, D.M. Smilgies, W.L. Cheng, 2D Freestanding Janus gold nanocrystal superlattices, Adv. Mater., 31 (2019) 1900989.

[43] H.K. Lee, Y.H. Lee, C.S.L. Koh, C.P.Q. Gia, X.M. Han, C.L. Lay, H.Y.F. Sim, Y.C. Kao, Q. An, X.Y. Ling, Designing surface-enhanced Raman scattering (SERS) platforms beyond hotspot engineering: emerging opportunities in analyte manipulations and hybrid materials, Chem. Soc. Rev., 48 (2019) 731-756.

[44] C. Hanske, E.H. Hill, D. Vila-Liarte, G. González-Rubio, C. Matricardi, A. Mihi, L.M. Liz-Marzán, Solvent-assisted self-assembly of gold nanorods into hierarchically organized plasmonic mesostructures, ACS Appl. Mater. Interfaces, 11 (2019) 11763-11771.

[45] R. Kullock, W.R. Hendren, A. Hille, S. Grafström, P.R. Evans, R.J. Pollard, R. Atkinson, L.M. Eng, Polarization conversion through collective surface plasmons in metallic nanorod arrays, Opt. express, 16 (2008) 21671-21681.

[46] G.A. Wurtz, R. Pollard, W. Hendren, G. Wiederrecht, D. Gosztola, V. Podolskiy, A.V. Zayats, Designed ultrafast optical nonlinearity in a plasmonic nanorod metamaterial enhanced by nonlocality, Nat. Nanotechnol., 6 (2011) 107-111.

[47] G. Pontifex, P. Zhang, Z. Wang, T. Haslett, D. AlMawlawi, M. Moskovits, STM imaging of the surface of small metal particles formed in anodic oxide pores, J. Phys. Chem., 95 (1991) 9989-9993.

[48] W. Ye, R. Long, H. Huang, Y. Xiong, Plasmonic nanostructures in solar energy conversion, J. Mater. Chem. C, 5 (2017) 1008-1021.

[49] L. Zhong, X. Zhou, S. Bao, Y. Shi, Y. Wang, S. Hong, Y. Huang, X. Wang, Z. Xie, Q. Zhang, Rational design and SERS properties of side-by-side, end-to-end and end-to-side assemblies of Au nanorods, J. Mater. Chem., 21 (2011) 14448-14455.

[50] H.-S. Park, A. Agarwal, N.A. Kotov, O.D. Lavrentovich, Controllable side-by-side and end-to-end assembly of Au nanorods by lyotropic chromonic materials, Langmuir, 24 (2008) 13833-13837.

[51] Z. Yin, W. Zhang, Q. Fu, H. Yue, W. Wei, P. Tang, W. Li, W. Li, L. Lin, G. Ma, D. Ma, Construction of stable chainlike Au nanostructures via silica coating and exploration for potential photothermal therapy, Small, 10 (2014) 3619-3624.

[52] P.K. Jain, S. Eustis, M.A. El-Sayed, Plasmon coupling in nanorod assemblies: Optical absorption, discrete dipole approximation simulation, and exciton-coupling model, J. Phys. Chem.

B, 110 (2006) 18243-18253.

[53] B. Nikoobakht, Z.L. Wang, M.A. El-Sayed, Self-assembly of gold nanorods, J. Phys. Chem. B, 104 (2000) 8635-8640.

[54] Y. Xie, S. Guo, Y. Ji, C. Guo, X. Liu, Z. Chen, X. Wu, Q. Liu, Self-assembly of gold nanorods into symmetric superlattices directed by OH-terminated hexa (ethylene glycol) alkanethiol, Langmuir, 27 (2011) 11394-11400.

[55] M. Anyfantakis, Z. Geng, M. Morel, S. Rudiuk, D. Baigl, Modulation of the coffee-ring effect in particle/surfactant mixtures: the importance of particle–interface interactions, Langmuir, 31 (2015) 4113-4120.

[56] X. Chen, S. Shen, L. Guo, S.S. Mao, Semiconductor-based photocatalytic hydrogen generation, Chem. Rev., 110 (2010) 6503-6570.

[57] S. Kou, W. Ye, X. Guo, X. Xu, H. Sun, J. Yang, Gold nanorods coated by oxygen-deficient TiO_2 as an advanced photocatalyst for hydrogen evolution, RSC Adv., 6 (2016) 39144-39149.

[58] B.-H. Wu, W.-T. Liu, T.-Y. Chen, T.-P. Perng, J.-H. Huang, L.-J. Chen, Plasmon-enhanced photocatalytic hydrogen production on Au/TiO_2 hybrid nanocrystal arrays, Nano Energy, 27 (2016) 412-419.

[59] Y. Niu, L. Sang, A contrastive study on the properties of plasmon-induced electrons generated from prism- and column-shaped nanoparticles, Phys. Chem. Chem. Phys., 22 (2020) 15463-15477.

[60] Z. Zheng, T. Tachikawa, T. Majima, Single-particle study of Pt-modified Au nanorods for plasmon-enhanced hydrogen generation in visible to near-infrared region, J. Am. Chem. Soc., 136 (2014) 6870-6873.

[61] Z. Yin, Y. Wang, C. Song, L. Zheng, N. Ma, X. Liu, S. Li, L. Lin, M. Li, Y. Xu, W. Li, G. Hu, Z. Fang, D. Ma, Hybrid Au–Ag nanostructures for enhanced plasmon-driven catalytic selective hydrogenation through visible light irradiation and surface-enhanced Raman ccattering, J. Am. Chem. Soc., 140 (2018) 864-867.

[62] M.D. Doherty, A. Murphy, J. McPhillips, R.J. Pollard, P. Dawson, Wavelength dependence of Raman enhancement from gold nanorod arrays: quantitative experiment and modeling of a hot spot dominated system, J. Phys. Chem. C, 114 (2010) 19913-19919.

[63] A. Martín, C. Schopf, A. Pescaglini, J.J. Wang, D. Iacopino, Facile formation of ordered vertical arrays by droplet evaporation of Au nanorod organic solutions, Langmuir, 30 (2014) 10206-10212.

[64] E. Hao, G.C. Schatz, Electromagnetic fields around silver nanoparticles and dimers, J. Chem. Phys., 120 (2004) 357-366.

[65] M. Valenti, M.P. Jonsson, G. Biskos, A. Schmidt-Ott, W.A. Smith, Plasmonic nanoparticle-semiconductor composites for efficient solar water splitting, J. Mater. Chem. A, 4 (2016) 17891-

17912.

[66] F. Rossella, P. Galinetto, M. Mozzati, L. Malavasi, Y. Diaz Fernandez, G. Drera, L. Sangaletti, TiO_2 thin films for spintronics application: a Raman study, J. Raman Spectrosc., 41 (2010) 558-565.

[67] G. Yu, J. Qian, P. Zhang, B. Zhang, W. Zhang, W. Yan, G. Liu, Collective excitation of plasmon-coupled Au-nanochain boosts photocatalytic hydrogen evolution of semiconductor, Nat. Commun., 10 (2019) 4912.

[68] A. Lee, G.F.S. Andrade, A. Ahmed, M.L. Souza, N. Coombs, E. Tumarkin, K. Liu, R. Gordon, A.G. Brolo, E. Kumacheva, Probing dynamic generation of hot-spots in self-assembled chains of gold nanorods by surface-enhanced raman scattering, J. Am. Chem. Soc., 133 (2011) 7563-7570.

Figures

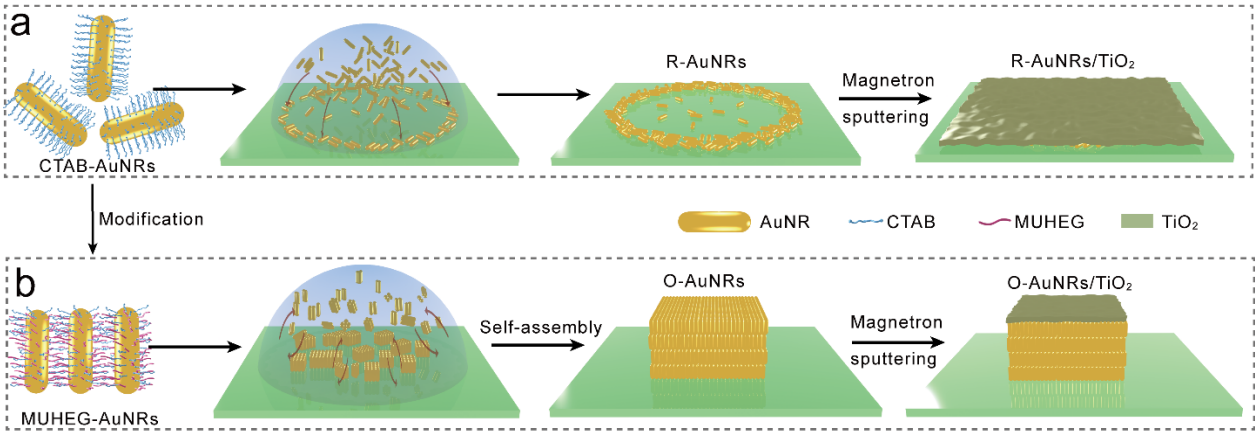

Fig. 1 Schematic diagrams showing the synthetic procedures of (a) R-AuNRs/TiO_2 and (b) O-AuNRs/TiO_2 films.

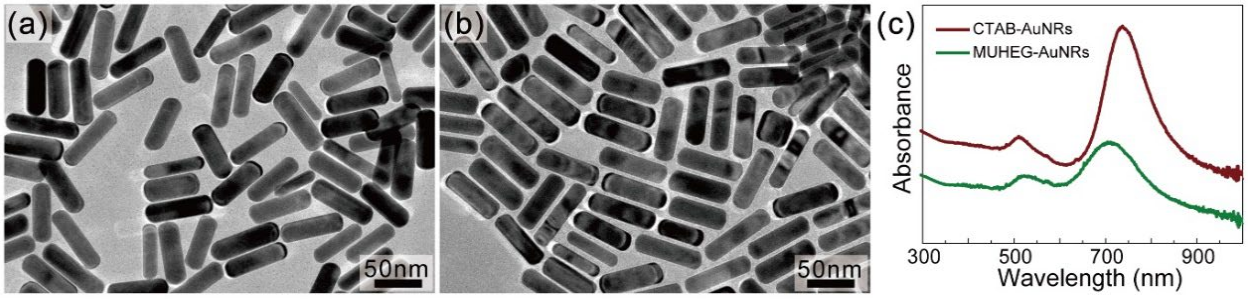

Fig. 2. TEM images of (a) CTAB-AuNRs, and (b) MUHEG-AuNRs. (c) UV-Vis-NIR absorption spectra of CTAB-AuNRs (wine line) and MUHEG-AuNRs (olive line) aqueous solutions.

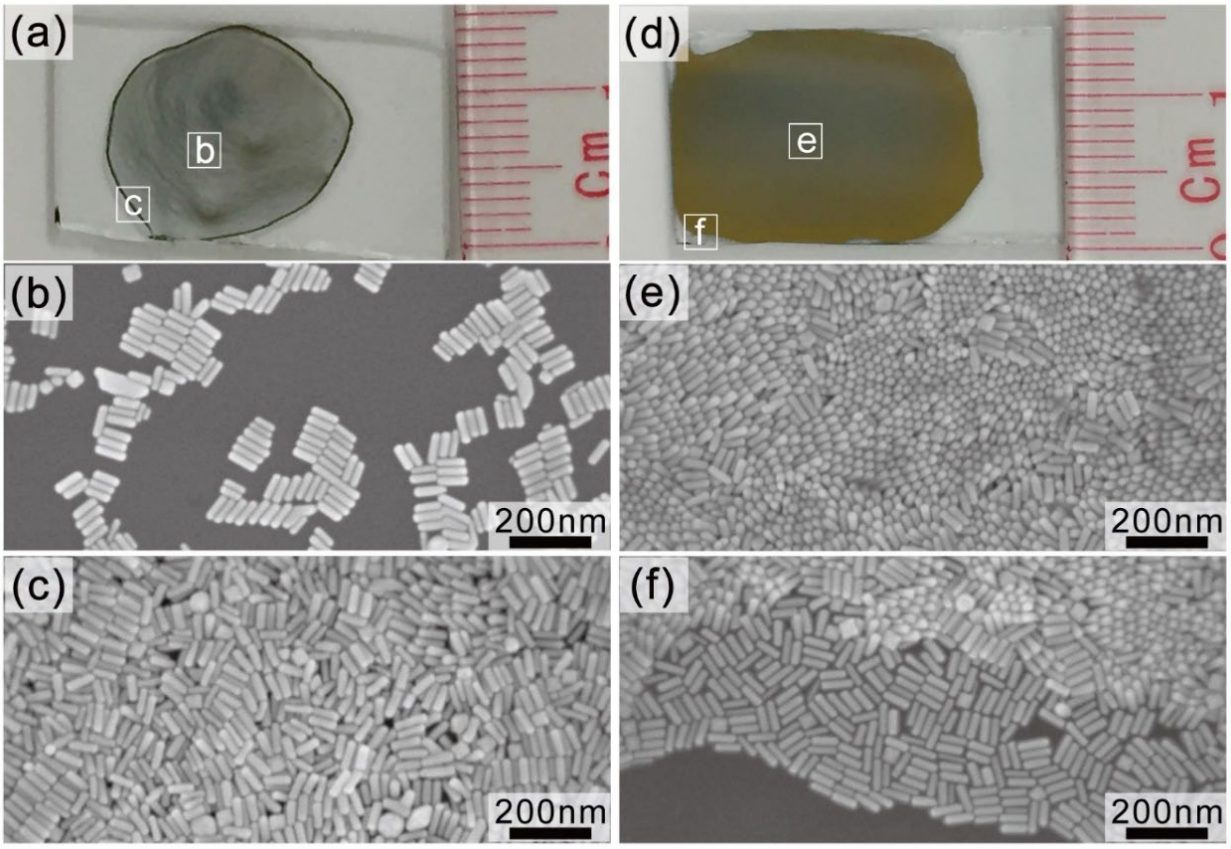

Fig. 3. Photographic images of AuNR assemblies obtained from the droplets of the same amount of (a) CTAB-AuNRs and (d) MUHEG-AuNRs on a glass slide. SEM images of (b) center and (c) rim of CTAB-AuNRs film, (e) center and (f) rim of MUHEG-AuNRs film on a glass. The areas selected for SEM analyses are marked in (a) and (d).

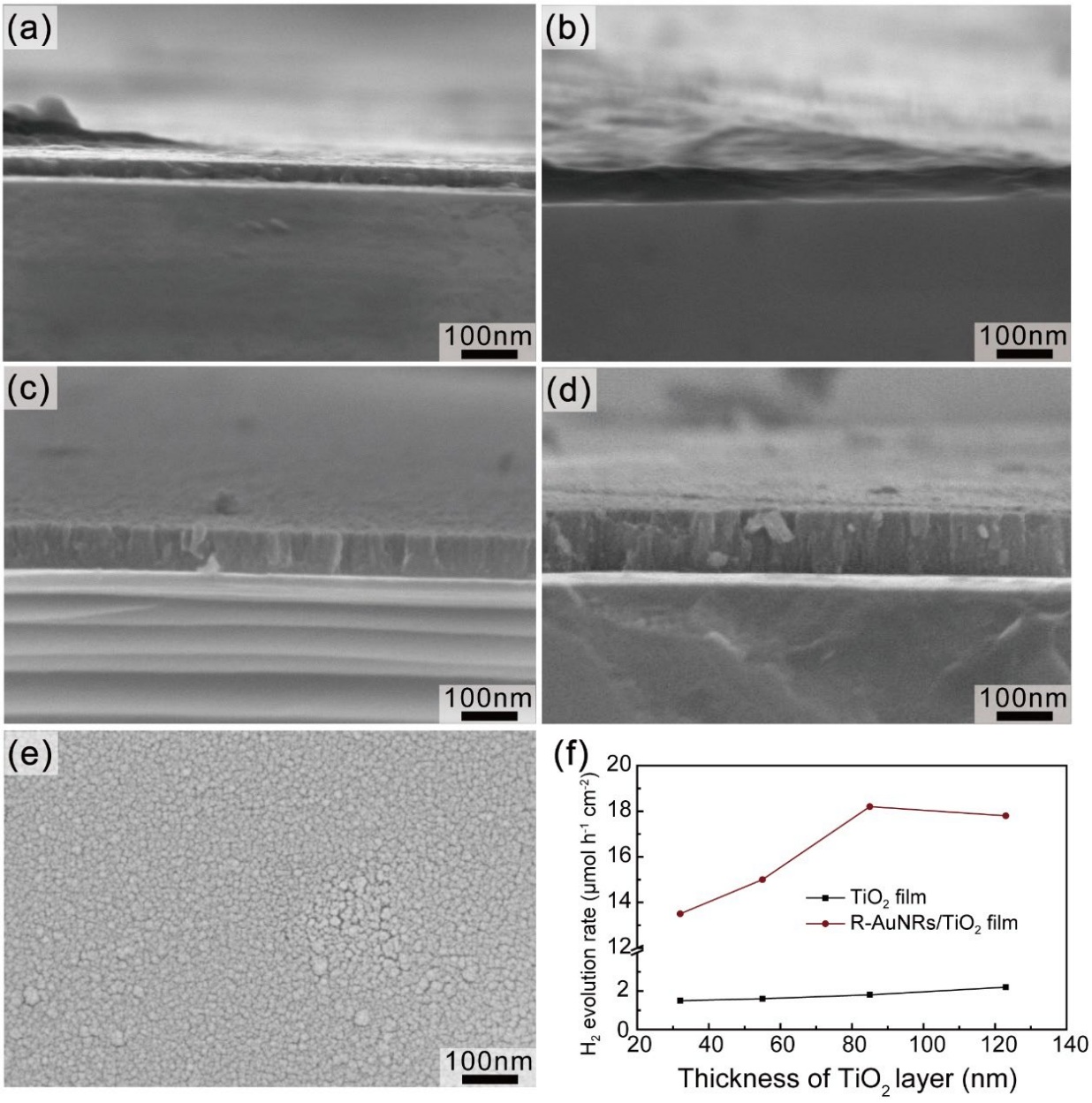

Fig. 4. Cross-sectional SEM images of the TiO_2 films with various deposition time: (a) 10 min, (b) 20 min, (c) 30 min, and (d) 45 min. (e) Top-view SEM image of the TiO_2 film deposited for 30 min. (f) Photocatalytic HER rates of TiO_2 (black line) and R-AuNRs/TiO_2 (win line) as a function of TiO_2 layer thickness.

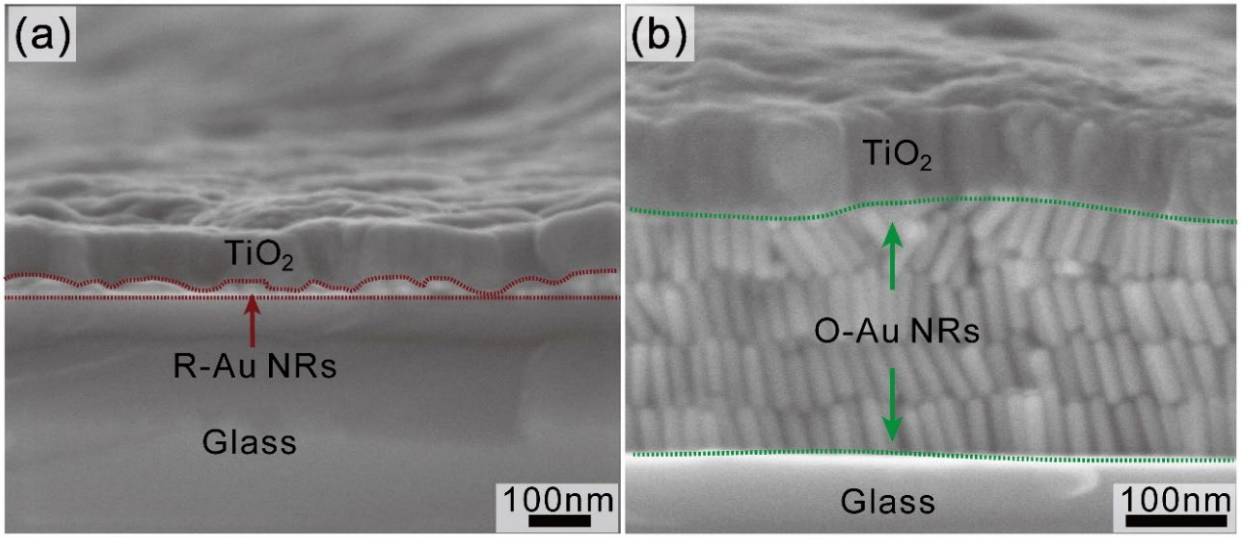

Fig. 5. Cross-sectional SEM image of the (a) R-AuNRs/TiO_2 and (b) O-AuNRs/TiO_2 films.

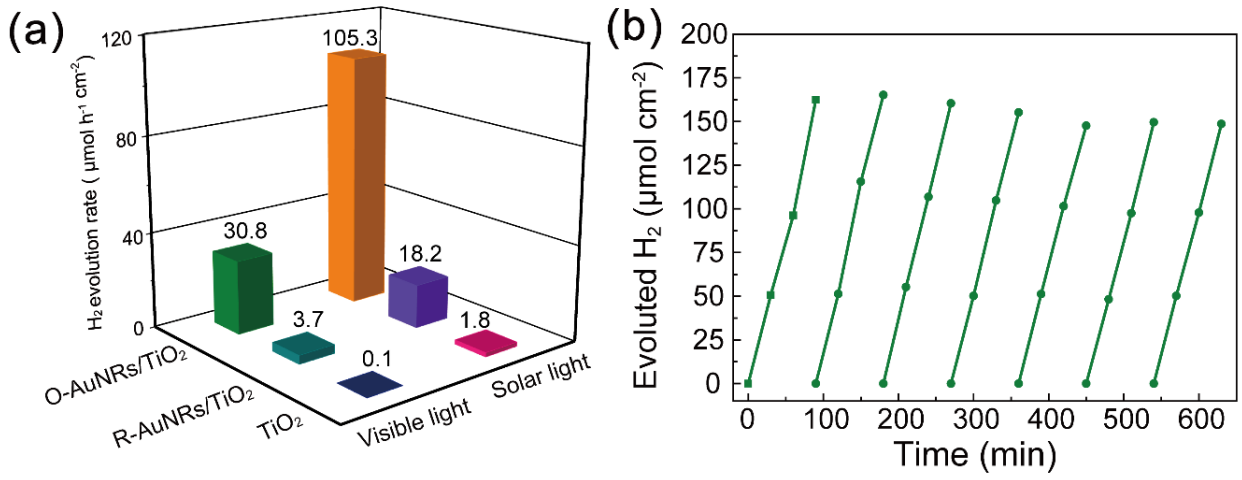

Fig. 6. (a) Comparison of the photocatalytic HER rates among the TiO_2, R-AuNRs/TiO_2, and O-AuNRs/TiO_2 films. (b) Long-term photocatalytic H_2 generation over the O-AuNRs/TiO_2 film.

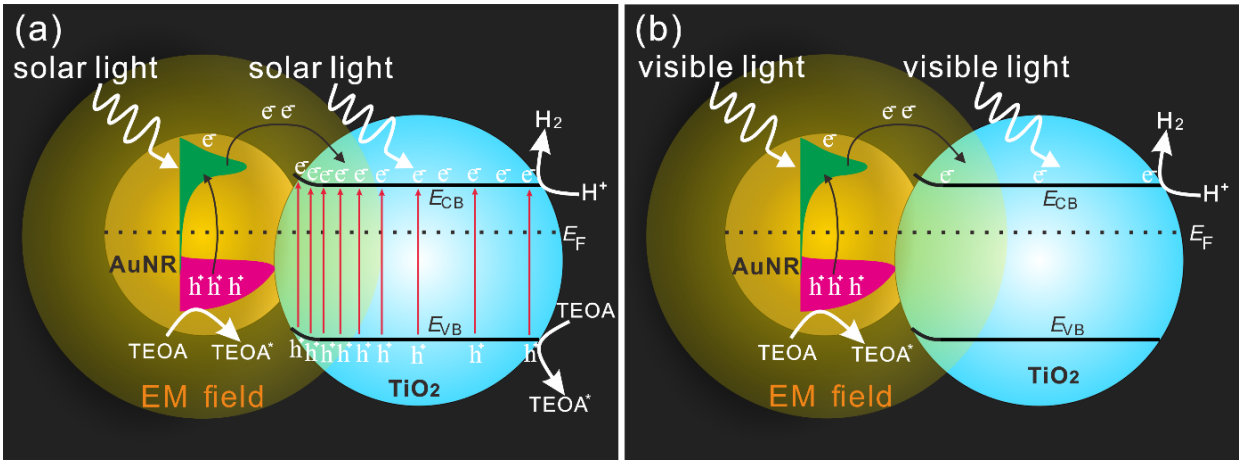

Fig. 7. Schematic diagrams showing the proposed photocatalytic HER mechanism of the AuNRs/TiO_2 films under (a) simulated solar light and (b) visible light irradiation. E_{CB} is the minimum energy level of conduction band and E_{VB} is the maximum energy level of valence band E_F represents the Fermi energy level and EM field is the electromagnetic field.

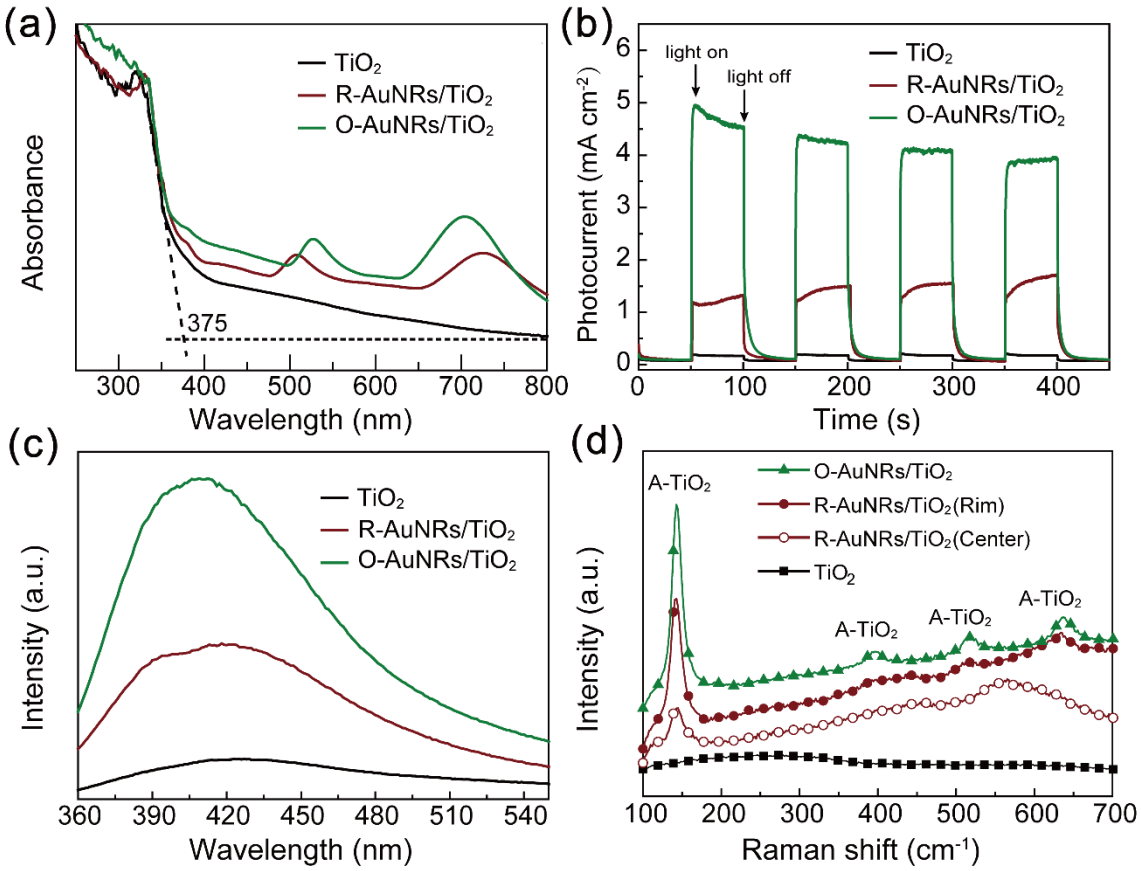

Fig. 8. (a) UV-vis diffuse reflectance spectra, (b) photocurrent response, (c) PL spectra, and (d) Raman spectra of the TiO_2, the R-AuNRs/TiO_2, and the O-AuNRs/TiO_2.

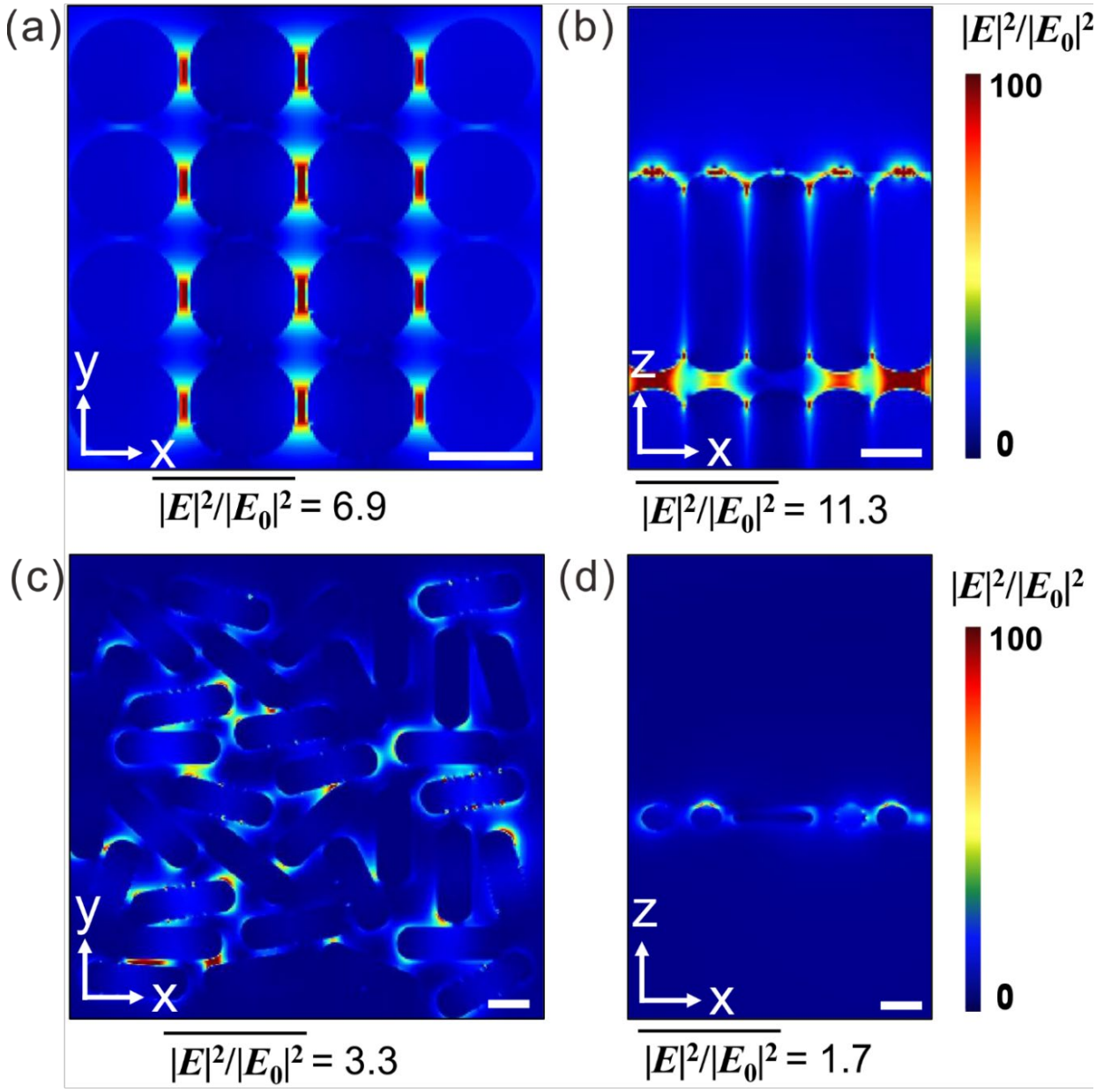

Fig. 9. Simulated local electromagnetic field intensity distributions of (a and b) O-AuNRs/TiO_2 and (c and d) R-AuNRs/TiO_2 films in the cross section, along x−y plane (a and c) and x−z plane (b and d). The $\overline{|E|^2 / |E_0|^2}$ is the averaged electric field intensity enhancement factor between the AuNRs and TiO_2 layer.